Chapter 5

Micromachined Infrared Detectors Based on Pyroelectric Thin Films

P. Muralt
Ceramics Laboratory, Swiss Federal Institute of Technology EPFL, Lausanne, Switzerland

An overview is given on infrared detector technology based on pyroelectric thin films. Pyroelectricity allows the realization of uncooled, thermal infrared detectors. The pyroelectric effect is introduced as well as the relevant materials family, namely the ferroelectrics. Properties are discussed in view of the infrared detector application. The product of dielectric constant and loss determine the intrinsic noise power of the pyroelectric element and must be kept under control while optimizing pyroelectric coefficients by materials choice and operating conditions. Two possible exploitation modes exist. In a first one, the true pyroelectric effect of a stable and poled ferroelectric element is employed. There is no need for temperature stabilization and the detector is operated at ambient conditions. In a second mode, ferroelectric materials are stabilized by an electric field closely above the para-to-ferroelectric phase transition in order to profit from the large and strongly temperature dependent anomaly related to the polarization fluctuations. This requires a precise temperature control and the phase transition must be of slight first order. An overview is given on pyroelectric thin film materials. Microstructural, process, substrate, and clamping effects are discussed. The physics of IR detectors for pyroelectrics is introduced highlighting the situations relevant for thin film detectors in theory and experiment. As thin film elements exhibit small thermal capacities, they are especially apt to be used at higher frequencies measuring the current response, provided that the thermal insulation of the element is well done. Micromachining is briefly introduced and some examples of realized detectors are given. The state of the art of applications is presented including point detectors for human presence sensors, linear arrays for gas spectroscopy, and two-dimensional focal plane arrays for thermal imaging. Finally, some comments are made on the potential of thin film pyroelectric devices.

1. Introduction

Pyroelectricity provides one of the best performing principles for the detection of temperature changes. It is a phenomenon of polar matter and results in the appearance of surface charges proportional to a temperature change ΔT. The basic structure is a planar capacitor whose charge Q varies according to $\Delta Q = Ap\Delta T$, where A is the area of the capacitor and p the pyroelectric coefficient. A pyroelectric sensor thus directly generates an electric signal, facilitating the integration into electronic circuits. Pyroelectric crystals, ceramics of ferroelectric materials, as well as polymers have therefore been used since the 1960's in *thermal* infrared (IR) detectors (see [1–3] for reviews), joining the earlier thermal IR detection techniques of bolometers and thermopiles (see [4] for a historical review on thermal infrared detectors). Since the late 1980's, pyroelectrics are also investigated in the form of thin films and integrated onto micromachined structures (see [5] for a review). Pyroelectricity thus made its way from a scientific curiosity known since 2500 years [6] to a very useful physical effect that for instance enables firemen to see through smoke.

2. Fundamentals

Pyroelectricity is the electrical response of a polar, dielectric material to a change in temperature. The origin of this effect lies in polar features that are lined up with the same orientation along at least one direction in the material. In polymers, the polar features are polar molecules or groups. One can thus identify microscopic dipoles (for a review, see [3]). In inorganic materials it is often not possible to identify dipoles. It is rather the anisotropy and anharmonicity of chemical bonds that causes the centre of gravity of the positives charges moving differently than the centre of gravity of the negative charges upon changing the temperature. An equivalent effect results if negative charges (electrons) from the negative ions move towards the positive ions by a charge transfer process. More insight into such mechanisms of covalent nature in ionic crystals have recently been gained by first-principle calculations [7]. In crystalline matter, *pyroelectricity* occurs in all materials with symmetries that allow the existence of a polar direction. No symmetry element may exist in the point group that inverts or rotates this direction by 180° (see, e.g, [8]). Such materials are also *piezoelectric*, i.e. they respond with an electric field to a change of the shape. From the 20 piezoelectric point groups, 10 are polar and allow for pyroelectricity (see Figure 1). The pyroelectric effect is anisotropic and depends on the directions of the electroded faces with respect to the crystal axes: $\boldsymbol{p} = (p_x, p_y, p_z)$. The highest pyroelectric coefficients are measured in *ferroelectrics.* In such substances there is a spontaneous electric polarization $\boldsymbol{P_s}$ that can be inverted by the application of an external electric field, and consequently is a measurable physical quantity. Upon heating up, $\boldsymbol{P_s}$ diminishes and becomes zero at the critical temperature of the ferroelectric—para-electric phase transition as depicted in Figure 2 for a second order phase transition. The symmetry group of the ferroelectric phase is a sub-group of the symmetry group of the para-electric phase, i.e. a number of symmetry elements are lost (certainly the inversion element, if present in the paraelectric phase). The direction of $\boldsymbol{P_s}$ is not uniquely defined. Turning an existing solution by

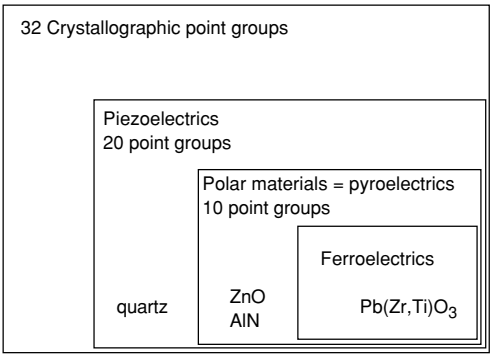

Fig. 1. Classification of space groups according to phenomena of polar symmetry including typical examples.

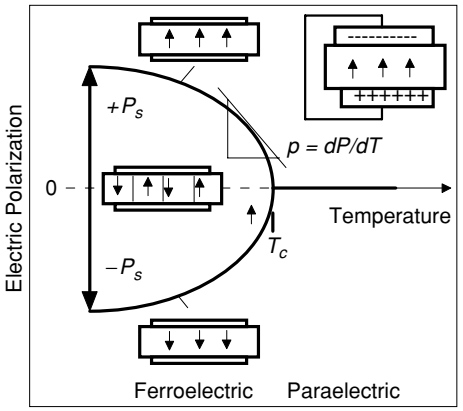

Fig. 2. Schematic graph showing the bifurcation (second order phase transition) of the electrical polarization at the critical temperature from $P = O$ (paraelectric phase) to the two equally probable solutions $+/-P_s$ for the spontaneous polarization in the ferroelectric phase. The inserted capacitors show extreme cases of 180° domain configurations.

180° (applying the lost inversion, mirror or rotation symmetry) yields always another, equally probable solution. Regions with homogeneous polarization are called domains. For achieving a macroscopic polarization, a poling process in an external electric field—often combined with heating above room temperature—must be applied to eliminate the 180° domains and to switch possibly also ferroelastic domains (as e.g. 90° domains). The macroscopic orientation obtained after removal of the external field is called remanent polarization $\boldsymbol{P_r}$.

The charges on the electrodes are given by the electric displacement field $\boldsymbol{D}$ perpendicular to the electrode faces. Giving the index 3 to this direction, the measured pyroelectric coefficient is equal to $\partial D_3 / \partial T$. The electric displacement field is be written as $\boldsymbol{D}(\boldsymbol{E}) = \varepsilon_0 \boldsymbol{E} + \boldsymbol{P}(\boldsymbol{E})$, where ε_0 means the permittivity of the vacuum. The in ferroelectrics polarization part is much larger and the only relevant temperature dependent

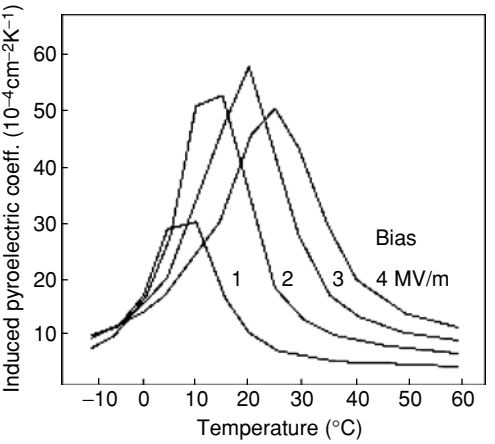

Fig. 3. Experimental curves for the induced pyro-electric coefficient in lead scandium tantalate (from [9]);

term. For the present discussion one can set $\boldsymbol{D}$ equal to $\boldsymbol{P}$.

$$\Delta D_3 = \frac{\partial P_3(E)}{\partial T}\Delta T \cong \frac{\partial P_{r,3}}{\partial T}\Delta T + \frac{\partial \varepsilon_{33}}{\partial T}E_3 \cdot \Delta T \tag{2.1}$$

The first term is called the true pyroelectric effect and $p_3 = \partial P_{r,3}/\partial T$ is the true pyroelectric coefficient. The second term arises from the first order correction for $P_r(E)$. Pyroelectricity arising due to this second term is called induced pyroelectricity. Accordingly there are two modes of operation for pyroelectric IR detectors. The first one works without external electric field at a temperature much below the para-to-ferroelectric phase transition. The polarization P_r (omitting the index 3 in the following) has previously been maximized by hot poling at an elevated electric field, assuring a good time stability of p at the application temperature around room temperature. The second mode exploits the peaking of p near the phase transition. A dc electric field needs to be applied to obtain a non-zero average polarization. One speaks of induced pyroelectric currents or sometimes of dielectric bolometer mode, since the field dependence of P can be considered as a dielectric property. The applied field has not only the effect of eliminating 180° domains, it broadens and shifts (first order transition only) the phase transition to higher temperatures. This leads to a reduction of the signal. There is thus an optimal dc field (a few MV/m) and temperature (see Figure 3) at which the response is peaking. The temperature of such a device needs to be stabilized. The advantage of the first method is the simplicity of operation conditions: no dc field and no temperature stabilization are needed. The second method allows higher sensitivities.

In the following the phenomenological theory of Landau, Ginzburg and Devonshire (LDG, see MS 435) is used to gain some better insight into the difference of true and induced pyroelectricity (using the notation in [10]) and to prepare the ground for

discussing materials figure of merits. The free energy density G of the ferroelectric phase is written as (monodomain, $\boldsymbol{P}$ perpendicular to electroded faces):

$$G(T, P) = \frac{1}{2}\beta(T - T_0)P^2 + \frac{1}{4}\gamma P^4 + \frac{1}{6}\delta P^6$$
$$E = \beta(T - T_0)P + \gamma P^3 + \delta P^5 \tag{2.2}$$

The derivation with respect to D yields the electric field E. The lowest energy at $E = 0$ yields the spontaneous polarization P_s. The inverse permittivity due to the ferroelectric effect is equal the second derivative of G with respect to D. A general relation is found for the *true pyroelectric coefficient* as follows: $p = -\beta\varepsilon P_s$. High pyroelectric coefficients are thus found in materials with high polarization and high coefficient β. The true pyroelectric *voltage response*, which is proportional to p/ε, follows the spontaneous polarization and is thus optimal at low temperatures, far below the phase transition. In case of a *second order phase transition* ($\gamma > 0$), and neglecting the sixth order term ($\delta = 0$), the spontaneous polarization is readily obtained as $P_s = (\frac{\beta}{\gamma}(T_0 - T))^{1/2}$. The true pyroelectric coefficient is derived as $p = \frac{-1}{2}(\frac{\beta}{\gamma(T_0-T)})^{1/2}$. The pyroelectric coefficient diverges at the phase transition temperature T_0. So does the permittivity, for which below the critical temperature T_0 the relation $\varepsilon^{-1} = \frac{\partial^2 G}{\partial P^2} = 2\beta(T_0 - T)$ is obtained. The pyroelectric coefficient obviously behaves as the square root of the permittivity, i.e. $\frac{p}{\sqrt{\varepsilon}} = -\beta\sqrt{\frac{2}{\gamma}} = const.$ In *ideal first order transitions* ($\gamma < 0, \delta > 0$) the critical temperature $T_c = T_0 + \frac{3\gamma^2}{16\beta\delta}$ is above T_0 and the polarization jumps form 0 to $\sqrt{-3\gamma/4\delta}$. The permittivity remains finite but jumps as well at T_c. The jump of P_s at T_c gives rise to large pyroelectric currents. Induced pyroelectricity is thus very large in materials with first order phase transitions. In addition, the field needed for induced pyroelectricity does not simply broaden the transition as in case of second order phase transitions, but the discontinuity of P is preserved up to a certain critical field [9]. The critical temperature is shifted to higher temperatures up to a maximal possible value of $T_{\max} = T_0 + \frac{9\gamma^2}{20\beta\delta}$. For illustration, calculated curves are depicted in Figure 4 for a model substance.

A further type of phase transitions that attracts attention for being used in the induced pyroelectric mode is the relaxor-ferroelectric transition. It occurs typically in specifically disordered ferroelectrics, where for instance the B-site of the perovskite ABO_3 is a mixture of randomly distributed ions of different valency. In the above mentioned $PbSc_{0.5}Ta_{0.5}O_3$, Sc^{+3} and Ta^{+5} ions occupy in a 1:1 mixture a site that should have a 4+ ion. If the two different ions are ordered in a periodic manner, the above discussed, ideal first order phase transition takes place, if they are disordered, the ferroelectric phase is shifted to lower temperatures [11]. Usually, very high low-frequency permittivities are obtained around the phase transition. It is thought that random internal fields prevent a homogeneous, ferroelectric polarization. Instead, local polar regions appear that easily grow in an external field thus providing for the huge dielectric response. There are chances that the absence of domain or phase fluctuations in the relaxor phase allow for working points with a larger dP/dT and a lower $tan\delta$. A modelling of this issue is missing to date.

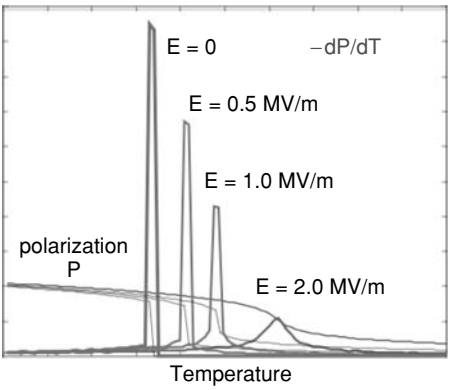

Fig. 4. Theoretical behavior of the pyroelectric coefficient as a function of temperature and for various electric fields, as derived from the Landau-Devonshire model. The behavior near the phase transition in absence of an external field is purely theoretical, since the average polarization decays to zero by thermal fluctuations.

The pyroelectric charge is usually not directly measured as a charge but as a current I trough a capacitor of surface A. Taking the time derivative of eqn 2.1:

$$I = A \cdot \frac{dD}{dt} = A \cdot p \cdot \frac{dT}{dt} \tag{2.3}$$

The current measurement is much less prone to drifts and also faster than charge measurements. In addition, charges are compensated with time because of leakage currents through the pyroelectric capacitor, or by conduction through air or along the device surface. For imaging static pictures or temperatures a chopper is applied that modulates the infrared radiation falling onto the detector with a constant angular frequency $\omega = 2\pi f$. The frequency f amounts typically to 30 to 60 Hz for imaging applications.

Several methods have been proposed for the measurement of the pyroelectric effect of bulk (see e.g. [6]) or thin film samples. The most frequently applied techniques are based on the pyroelectric current generated by a temperature ramp of constant rate (i.e. $dT/dt = \text{const}$), yielding a constant pyroelectric current according to eqn 2.3. One speaks of the Byer-Roundy technique when a single ramp is applied. It is important to check heating and cooling curves, because the release of trapped charges (thermally induced currents) might falsify the heating curve. Such trapped charges are injected into the sample during the poling procedure. An improvement of the method is obtained by cycling the temperature periodically. The temperature is swept up and down with small amplitudes (e.g. 1 K) and with constant rates (e.g. 0.2 K/s) around a given average temperature. The pyroelectric current, being proportional to the slope of the temperature, will switch between two constant values after some stabilization time. The temperature is best controlled on a small chuck equipped with Joule heating and Peltier cooling elements, placed in a chamber protecting from perturbations [9, 12]. For higher modulation frequencies, temperature changes are induced by chopped light absorption (Chynoweth). However, this technique is more qualitative than quantitative because it requires the knowledge of thermal properties for deriving the actual temperature (see

the next section). Sometimes the polarization is measured as a function of temperature. This is rather dangerous, since the polarization must be derived from a hysteresis loop obtained by switching the polarization. Firstly, it is not sure whether the complete polarization is switching, secondly fatigue could reduce polarization more efficiently than the temperature increase.

The quality of a sensor does not only depend on sensitivity, but also on the signal-to-noise ratio (S/N ratio), or in other words, the noise level. The intrinsic noise type of pyroelectrics is the Johnson noise of the capacitor element (see, e.g., [1, 2]). For a capacitor of area A and thickness t, the noise current is obtained as:

$$I_n = \sqrt{\frac{A}{t} 4kT\,(\sigma + \omega\varepsilon \tan\delta)\,\Delta f} \tag{2.4}$$

where σ is the leakage conductivity of the pyroelectric thin film (in bulk detectors: the parallel resistor), ω the angular frequency, $tan\sigma$ the loss tangent, Δf the frequency bandwidth, A the surface, and t the thickness of the element. The cross over frequency $\omega_{\mathrm{cn}} = \sigma/(\varepsilon \cdot tan\sigma)$ between resistor type noise and dielectric noise amounts to typically 0.1–10 Hz. At usual modulation frequencies of 10 to 60 Hz the dielectric noise is thus dominating. The intrinsic figure of merit of the dielectric and pyroelectric materials parameters for an optimal S/N ratio can thus formulated as:

$$FM = \frac{p}{\sqrt{\varepsilon \tan\delta}} \tag{2.5}$$

Various phenomena can contribute to the dielectric loss. At high frequencies (GHz and higher) the dielectric loss increases due to interactions of phonons and ac electric fields (see [13] and [14]). In non-centro-symmetric materials the dominating phonon mechanism is the quasi-Debye loss mechanism. Thermal fluctuations and relaxation of phonons lead to charge fluctuations in a similar way as dipoles give rise to loss in the Debye theory. In ferroelectrics, domain wall relaxations play a role as well. In the 1 to 10 GHz range there is usually a relaxation of 180° domain wall motions. All these mechanisms yield a $tan\delta$ that increases at least linearly with the dielectric constant, i.e. $\tan\delta \propto \varepsilon^{\alpha}$, where a is between 1 and 4 [13]. It is difficult to make a general theory on loss mechanisms at the very low frequencies of a few tens of Hertz. In this region dielectric loss is governed by defects and ferroelectric domains. Charged or dipolar point defects relax with respect to position or orientation, structural defects may interfere with electric fields by means of the piezoelectric coupling, and defects may delay domain wall motions or give rise to a creeping of domain walls. Many of the low frequency relaxation mechanisms show again a $tan\delta$ proportional to ε. Near the critical temperature, polarization fluctuation and phonon losses (soft mode) were found to follow a Curie-Weiss law like the dielectric constant, meaning that $tan\delta$ diverges as well at the critical temperature. This has for instance been found in ref [9] where the loss tangent and the dielectric constant increase by abut the same factors upon approaching the critical temperature ($PbSc_{0.5}Ta_{0.5}O_3$). The materials figure of merit FM behaves thus rather like $p\varepsilon^{-1}$ than $p\varepsilon^{-1/2}$ especially near critical temperatures.

Evaluating the FM by means of the LDG theory leads to the conclusion that in case of second order phase transitions there is no improvement of the intrinsic signal to noise ratio when going closer to the phase transition. $p\varepsilon^{-1/2}$ is in fact independent of

temperature and taking into account the increasing dielectric losses, the intrinsic signal to noise is expected to decrease with temperature. The case of first order transitions is more difficult to judge. The permittivity does not diverge at the phase transition, there is only a discontinuity. Lead scandium tantalate showed an increase of *FM* of nearly a factor 3 [9], hence a clear advantage for induced pyroelectricity in this case. The optimal dc field is, however, not the one at which the pyroelectric current is peaking, i.e. inside the hysteretic first order transition with mixed phase noise, but just somewhat above the critical field at which the jump in polarization is lost.

3. Operation Principles of Pyroelectric Infrared Detectors

The main application of pyroelectric materials is detection of infrared (IR) radiation. The latter is measured indirectly by means of a temperature change ΔT of an absorbing structure as a result of the absorbed radiation power. The thermal properties of the absorbing structure have to be suitably designed for obtaining a maximal temperature increase ΔT at the required response frequency. ΔT is obtained from the balance of the heat flows, as sketched in Figure 5. First of all, some fraction η of the infra-red radiation (power W) falling onto the element is absorbed, i.e., transformed into heat. The temperature change at a given heat input $\eta \cdot W \cdot \Delta t$ depends on the heat conductivity G to the surrounding heat reservoir (heat sink) at temperature T_O and the heat capacity H of the element. It is supposed that the element exhibits a uniform temperature. Thermal wavelength effects are thus neglected. This is justified in thin structures with uniform illumination by the IR radiation. (In $PbTiO_3$ with specific heat capacity $c_p = 3.2$ MJ/m^3/K and specific heat conductivity $\kappa = 3.8$ W/m/K, the thermal wavelength amounts to 600 μm at 1 Hz and 20 μm at 1 kHz.) Considering stationary solutions in the frequency domain for an IR power of $W = W_\omega \cdot e^{i\omega t}$, the temperature modulation is readily obtained as:

$$\Delta T_\omega = \frac{\eta \cdot W_\omega}{G + i\omega \cdot H}, \quad |\Delta T_\omega| = \frac{\eta \cdot W_\omega}{G\sqrt{1 + \omega^2 \cdot \tau_{th}^2}} \tag{3.1}$$

The thermal time constant $\tau_{th} = H/G$ has been introduced. There are thus two frequency domains separated by the inverse thermal time constant. The *current responsivity*, i.e. the current response per Watt of radiation power falling onto the detector

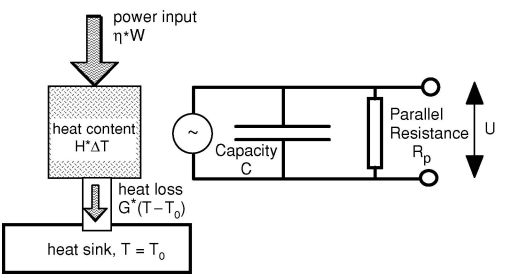

Fig. 5. Schematic of thermal and electrical circuit of a pyroelectric element.

element is obtained as:

$$\Re_J(\omega) = \frac{J_\omega}{W_\omega} = \frac{p \cdot \eta \cdot \omega \cdot A}{G\sqrt{1 + \omega^2 \cdot \tau_{th}^2}} \tag{3.2}$$

Alternatively, the voltage across a parallel resistor R_p can be measured. In bulk devices, a value of 10 G W is typically applied (R_p should not exceed the gate impedance of the amplifier.) In thin film devices, leakage through the film may yield an R_p in a good value range. At higher frequencies the dielectric loss tangent *tan d* comes also into play. The conductance Y of the complete element (thus including the parallel resistance) is obtained as:

$$|Y(\omega)| = \frac{1}{R_p}\sqrt{(1 + \omega \cdot \tau_{el} \cdot \tan\delta)^2 + \omega^2 \cdot \tau_{el}^2} \tag{3.3}$$

The electrical time constant $\tau_{el} = R_p \cdot C$ has been introduced. The voltage response is proportional to the impedance $Z = Y^{-1}$. Above the angular frequency τ_{el}^{-1}, the impedance decreases as ω^{-1}. The pyroelectric element thus works like a low pass filter, cutting off the high frequency voltage response. Omitting the small term in *tanδ,* the complete voltage responsivity is written as:

$$\Re_V(\omega) = |Z(\omega)| \cdot \Re_J(\omega) = \frac{p \cdot \eta \cdot \omega \cdot A \cdot R_p}{G \cdot \sqrt{1 + \omega^2 \cdot \tau_{th}^2} \cdot \sqrt{1 + \omega^2 \cdot \tau_{el}^2}} \tag{3.4}$$

The general trends of the two responsivity functions depend on the relative size of the two time constants. In *bulk devices* one generally encounters $\tau_{el} < \tau_{th}$ [1, 15]. The inverse situation, i.e. $\tau_{el} > \tau_{th}$ is typically thin film structures [16]. The resultant frequency behavior for thin films is schematically shown in Figure 6. In thin film devices the parallel resistance is not directly involved in the *voltage response*. This is very advantageous, as film leakage is not easy to control precisely. The mounting of parallel resistors can be avoided if the leakage is sufficiently large to avoid discharging through the input gate of the voltage amplifier. Observing that $C = \varepsilon A/t_p$ we can further develop the response in the intermediate region as $\Re_v \cong \frac{\eta \cdot p \cdot t_p}{\varepsilon \cdot G}$ in case of thin films, and $\Re_v \cong \frac{\eta \cdot p \cdot A \cdot R_p}{H}$ in the bulk case. The figure of merit given in general, $F_V s = \frac{p}{\varepsilon c_p}$, corresponds to a mix of those two situations, and is relevant in any case for the high frequency case. It includes both, dielectric constant (not that $\varepsilon = \varepsilon_0 \varepsilon_r$) and specific heat capacity c_p. For the thin film situation $F_V^* = p/\varepsilon$ is correct at the peaking of the voltage response. A small thickness is favorable to drive the current response up. The impact of the heat conductivity G at intermediate and low frequencies, and its unimportance at high frequencies, is demonstrated in Figure 7, which depicts the response of a pyroelectric detector in air and in vacuum, i.e. once with air convection (large G), and once without air convection (small G).

The *ultimate detection limit* of a sensor is given by the intrinsic noise of the detector element. In order to reach this limit with the complete sensor set-up, the noise contribution from the amplifier and from external sources of the environment have to be smaller than the intrinsic noise. Using low-noise amplifiers like J-FET transistors, the

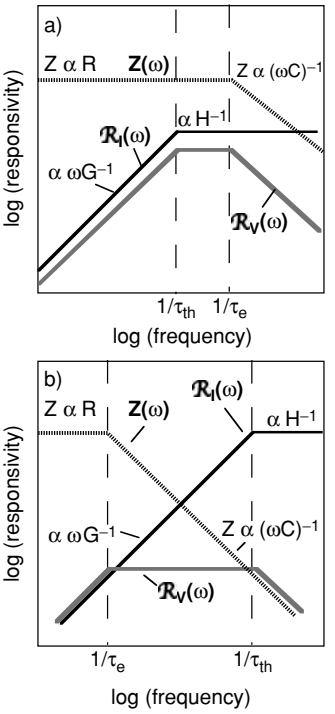

Fig. 6. Log-log scheme of current and voltage response, together with the impedance for the typical bulk (top) and thin film situation (bottom).

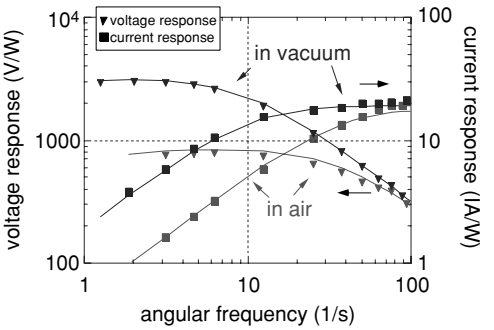

Fig. 7. Voltage and current responsivity of a linear array element (1 × 12) measured in air and in vacuum. One element was 0.4 × 0.9 mm large. The curves are calculated according to eqns 3.4 and 3.6, the points are measured ([16]).

theoretical limit of the intrinsic noise can indeed be reached. The thermal noise power $P_{thn} = \sqrt{4kT^2GB}$ is proportional to the square root of the heat conduction G, and is very small for optimized thin film devices. The Johnson noise is normally dominating. The contributing noise sources are given by the real part g of the admittance Y. The

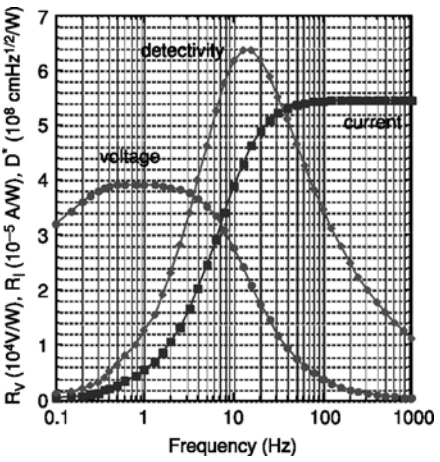

Fig. 8. Calculated responsivities and detectivity for a 0.01mm^2 large PLT element, taking typical published parameters (from [5]).

noise current J_n for a bandwidth B is obtained as:

$$J_n = \sqrt{4kTgB} \quad with \quad g = R_p^{-1} + \omega C \tan\delta \tag{3.5}$$

The minimal detectable power is the noise equivalent power defined by $NEP = J_n/\Re_J$. Very often, the detectivity D^* is given instead of the NEP:

$$D^* = \frac{A^{1/2}B^{1/2}}{NEP} = \frac{\Re_J(\omega) \cdot A^{1/2}B^{1/2}}{J_n} \tag{3.6}$$

The multiplication with $A^{1/2}B^{1/2}$ cancels surface and bandwidth contribution from the noise. At high frequencies, D^* is independent of detection area and bandwidth. For this reason D^* is frequently used as a measure of performance to compare different detectors. The best operating conditions are found near the inverse thermal time constant, where the signal to noise ratio is peaking (see Figure 8). Ideally, τ_{th} should be matched to $\tau_{el} \cdot \tan\delta$. The materials figure of merit for the detectivity is generally given as:

$$F_D = \frac{p}{c_p\sqrt{\varepsilon \tan\delta}}. \tag{3.7}$$

The detectivity D^* is a useful quantity to characterize an IR detector independently of size and detection bandwidth. However, for thermal imaging applications, D^* alone does not sufficiently characterize the complete device, which also contains an optical part. The quantity of interest is the minimal temperature difference of a black body target object with respect to the background temperature one still can detect. It is called the "noise equivalent temperature difference", NETD. The procedure to evaluate this quantity is as follows: The noise voltage V_n of the detector is measured when the target temperature is in equilibrium with the background temperature. The target temperature is increased by ΔT and the signal voltage $V_s(\Delta T)$ is measured. The NETD is derived

as [17]:

$$NETD = \frac{\Delta T}{V_s / V_n} \tag{3.8}$$

ΔT is equal to the NETD if the signal is just equal to the noise voltage. Of course, the NETD can be related to the NEP and D^* of the detector knowing the optical properties of the imaging system. The temperature increase ΔT has to be such that the increase of the power falling onto one pixel of the focal plane array (FPA) equals the NEP. The power increase is proportional to $\frac{dW}{dT}\Delta T$ in the wavelength interval $\Delta\lambda$ detected, where W is the power density emitted by the target surface. It is further proportional to the FPA pixel area A_D, and the transmissivity τ of the optics. The reader is referred to special literature on this topic [17] for the derivation of general formulas. The formula given below finds frequent use [18]:

$$NETD = \frac{(4F^2 + 1)}{A_D \cdot \tau \cdot (dW/dT)_{\Delta\lambda}} \cdot NEP = \frac{(4F^2 + 1)}{A_D^{1/2} \cdot \tau \cdot (dW/dT)_{\Delta\lambda}} \cdot \frac{B^{1/2}}{D^*} \tag{3.9}$$

F is the f-Number of the optics. Typically, a NETD of less than 100 mK is required for uncooled IR-imaging systems [19].

4. Thin Film Materials

4.1. Properties and figure of merits

Properties of thin film materials differ from those of bulk materials in as much as microstructure and substrate influence are of importance. Table 1 contains a list of representative materials and their characteristics for pyroelectric applications. It can be noted that thin film materials show as good characteristics as bulk materials, especially when they are grown epitaxially. In contrast to bulk ceramics, thin films can be grown textured or even completely oriented in the case of epitaxy. The optimal texture is achieved when the polar axis (polarization) stays perpendicular to the electrodes everywhere in the film. In this case, a performance similar to the one of single crystal materials is obtained. This leads to a considerable improvement of properties in the case of substances that only exist as polycrystalline ceramics in bulk form (as e.g., PZT, PLT). A good demonstration of this case is epitaxial $PbTiO_3$, whose figure of merit F_V^* was measured as 291 $kVm^{-1}K^{-1}$ [20] at thin films, whereas only 107 $kVm^{-1}K^{-1}$ is reached in bulk ceramics.

The discussion of bulk material properties made clear that there is a trade off between temperature stability and size of the pyroelectric effect. If a cheap, simple and reliable device is the goal, materials with high critical temperatures (T_c) such as $LiTaO_3$ and $PbTiO_3$ are more adequate. If the operating temperature can be held precisely, close to or exactly at the critical temperature, materials with near room temperature T_c, with ideal first order or relaxor-type behavior, yield much larger responses. The materials choice taken in the published thin film work indicates that $PbTiO_3$ derived compounds are the clear favorites until now, and much less work has been spent on the second category

Table 1. Bulk and thin film pyroelectric materials (sources: [1–3, 5, 21]. The figure of merits F_V, and F_D are given in the text

Material	p $[\mu Cm^{-2}K^{-1}]$	e_r	tand	c_p $[10^6 Jm^{-3}K^{-1}]$	F_V $[m^2C^{-1}]$	F_D $[10^{-5}Pa^{-1/2}]$	T_c [°C]
$LiTaO_3$, single crystal	230	47	< 0.01	3.2	0.17	5–35	620
$PbZrTiO_3$ (PZFNTU) bulk ceramic	380	290	0.003	2.5	0.06	5.5	230
$PbTiO_3$, bulk ceramics	180	190	0.01	3.0	0.04	1.5	490
$PbTiO_3$ (PCWT4-24) bulk ceramic	380	220	0.01	2.5	0.08	3.4	255
P(VDF/TrFE) 80/20 co-polymer film	31	7	0.015	2.3	0.22	1.4	135
PZT 15/85 (111) polycrystalline thin film on silicon (MEMS)	160–220	200–230	0.01–0.015	2.7	0.03–0.04	1.3–1.5	∼420
$PbLaTiO_3$ 10–20% La polycrystalline thin film on silicon	200–576	153–550	0.01–0.024	2.7	0.02–0.15	0.7–4.1	
$PbTiO_3$ (001) thin film epitaxy on Pt/MgO	250	97	0.006	3.2	0.09	3.4	∼490

of materials (see citations in [5]). Pure $PbTiO_3$ has been mostly abandoned because of too high dielectric losses and difficulties to pole. The most advanced integration work on silicon has been achieved with PZT (15 to 30 %) Zr films. This is a kind of spin-off from the work done in ferroelectric memories and actuators. The results collected in table 3 suggests that PZT is going to be replaced by PLT or PCT. The table also reveals that the research in $LiTaO_3$ thin films for pyroelectric applications is far away from being as advanced as its applications in bulk detectors. In general, films grown in epitaxial quality on single crystal substrates such as MgO, $SrTiO_3$ or sapphire exhibit figures of merit that are roughly two times higher than the ones of films deposited onto silicon. The reason for that will be discussed below. The earlier work on relaxor-type materials and lead scandium tantalate (PST) dealt with depositions on inert substrates only. Only recent efforts have been successful using ordinary platinized silicon substrates. The properties are, however, by a factor 3 to 10 lower. Main problem are the higher nucleation and growth temperatures as compared to lead titanate family, resulting in a degradation of the platinum bottom electrode and its interfaces. Suitable seeding layers [22–24] are applied to lower the nucleation temperature. Improvements in sol-gel chemistry still seem to be possible. Nevertheless it looks difficult to synthesize PST without second phases and with B-site ordering below 700 °C [25]. Low deposition temperatures have been achieved by MOCVD, however, no material properties were reported [26]. Comparing results obtained on equivalent substrates, one observes that induced pyroelectricity did not prove to be superior to the best PLT or PCT thin films showing the true pyroelectric effect so far (with the possible exception of PMZN).

For low frequency applications, thicker pyroelectric films might offer an advantage, since the voltage response increases with increasing thickness. Using thin film deposition techniques, ferroelectric thin films on silicon crack above 2 to 3 μm thickness, typically. The range of 5 to 20 μm is more apt for so-called thick film techniques. A slurry containing pyroelectric particles is deposited by screen printing on a substrate before drying and annealing. The published work (see table 6) indicates, however, a loss in performance by a factor 2 to 3. In addition, it is quite difficult to combine silicon micromachining techniques with thick film techniques. Most interesting looks the composite approach. The dilution of the pyroelectric material seems to reduce the dielectric constant much more than the pyroelectric coefficient, yielding a large $\Re_V$ [27].

Finally, it has to be mentioned that in some of the works the pyroelectric current has been measured, without determining the pyroelectric coefficient, so for $NaNO_2$ [28], and $LiTaO_3$ [29].

The figure of merit F_D has been determined very rarely by experiment. In most cases, it is just calculated using a literature bulk value for the volume heat capacity c_p. The values reported in table 1 are copied from the cited literature or else, calculated using reasonable values for c_p.

4.2. Substrate effects

Thin film materials cannot be considered independently from the substrate on which they are grown. The substrate may well influence microstructure and properties of the ferroelectric thin films. Three types of substrate influence can be identified:

(1) Growth phenomena related to the surface on which the film is grown (usually the bottom electrode).
(2) Thermal strains imposed by the bulk of the substrate during cool down from the growth temperature (the substrate during growth is typically is 100 to 1000 times thicker than the film).
(3) Thermal expansion mismatch with thin film support during operation of the pyroelectric film yielding a piezoelectric contribution to the pyroelectric effect.

The chemical nature, lattice and microstructure of the growth-substrate have important impacts on the nucleation of the films in general. The ferroelectric materials considered here often exhibit a pronounced nucleation controlled growth. This means that considerable activation energies are needed for nucleation of the correct phase, so for instance in case of PZT [30]. The growth-substrate may thus have a seeding function. If it is possible to reduce the interface energy for a given orientation, the nucleation energy is reduced for this given orientation and textured films can be obtained. This can be exploited to obtain a higher pyroelectric coefficient. The capability to grow one or the other orientation of $PbTiO_3$ derived compounds on platinized silicon substrates is an important issue of ferroelectric film integration. It is generally found that the (100)/(111) texture ratio is controlled by the Pb/Ti ratio during nucleation. This ratio is either influenced through growth parameters (e.g., high temperature favors Ti, thus (111)-orientation) or by suitable seed layers, such as a nanometer thick Ti or TiO_2 layer, leading to a (111)-orientation [31, 32]. Thin $PbTiO_3$ $\{001\}$ layers of some 10 nm may be used to seed perovskite (100) orientation [33, 34].

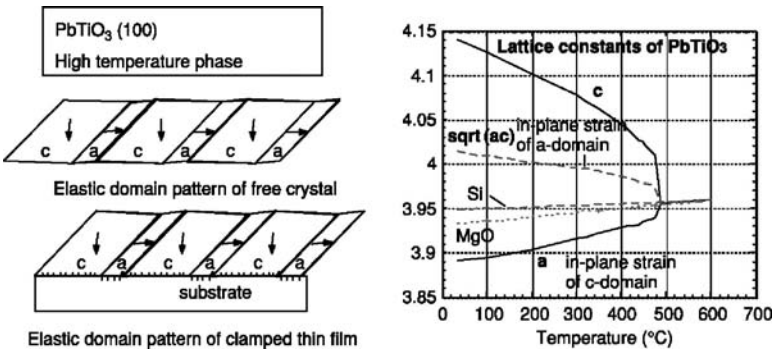

Fig. 9. Schematics showing domain formation in tetragonal {100} thin film together with spontaneous strains of $PbTiO_3$. Clamping to substrate induces angular distortions and dislocations.

Pyroelectric thin films of the perovskite family are typically grown at 500 to 700 °C in the paraelectric phase. The para-to-ferroelectric phase transition occurs when cooling down from the growth temperature. The best-suited true pyroelectrics known to date are all tetragonal materials derived from $PbTiO_3$, a material with a large polarization and large spontaneous strains (see Figure 9). The tetragonal and polar c-axis grows with decreasing temperature, the *a*-axis shrinks. If the film would be a homogeneous and free crystal, the c-axis would point with equal probability of $^1/_3$ along one of the former cubic axis resulting in a pattern of 90° domains. If during poling, 180° switching occurred exclusively, a maximal polarization of $P_s/3$ could be expected at best along one of the former cubic axis. The thin film case is much more complex. Very close to the substrate (bottom electrode) epitaxial relationships are established between the perovskite and the substrate lattice. The epitaxial misfit might be higher for one axis than for the other. For instance the *a*-axis of $PbTiO_3$ ($a = 3.96$ Å) is closer to the lattice constant of platinum (3.92 Å) than the c-axis of $PbTiO_3$ (4.14 Å). The interface $PbTiO_3$/Pt thus has lower energy with (001) planes than with (100) planes of $PbTiO_3$. For the bulk of the film, it is rather the average elastic energy due to misfit strains with the bulk of the substrate (as e.g., silicon) that needs to be minimized. In the ordinary case this happens by introducing misfit dislocations. However, in materials with ferroelastic domains, elastic energy can also be released by appropriately changing the volume fraction of the different types of domains [35]. The creation of domain walls is in competition with the creation of dislocations. The phenomenon has been studied mostly at the epitaxial system $PbTiO_3\{100\}/SrTiO_3(100)$ [36–43] and $PbTiO_3\{100\}$/MgO [44].

In order to achieve more than $P_s/3$ polarization of a {100}-oriented $PbTiO_3$ film, it is necessary that the misfit strains with the substrate are negative (the film is compressed), which results in an increase of c-domains. This mechanism is especially effective in a temperature interval just below the critical temperature, as nicely demonstrated in Figure 10. Ideal for a good c-axis orientation is a compressive stress of the film at the phase transition which may happen in the system $PbTiO_3\{100\}$/MgO. Well *c*-axis oriented films are thus obtained on $SrTiO_3$ [45] and MgO substrates [20] (see also table 4). Such a stress is built up during cool down from the growth temperature to the phase transition if the thermal expansion coefficient of the substrate is larger than

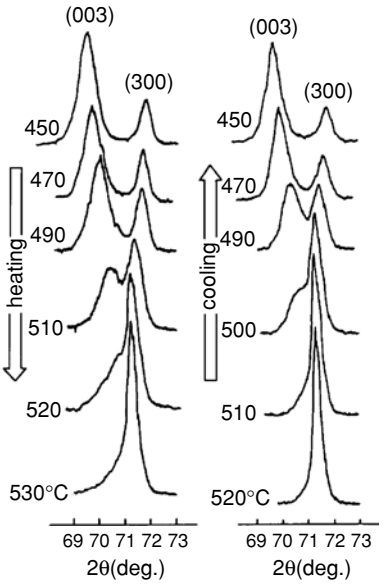

Fig. 10. X-ray diffraction intensities of (003) and (300) reflections as a function of temperature for epitaxial $PbTiO_3$ thin films grown on Pt(100)/MgO(100) ([20]).

the one of the paraelectric $PbTiO_3$. Residual growth stresses such as tensile stresses after crystallization of sol-gel processed films play a role as well. The domain issue is an important technological problem. The final goal is mostly the integration onto silicon substrates, which is a stringent condition for combining sensor and electronics on the same chip. However, for optimal polarization in tetragonal ferroelectrics such as $PbTiO_3$, silicon has a too low thermal expansion coefficient. Other substrates like MgO yield superior results. For small arrays only, a hybrid approach might be acceptable. MgO is a suitable substrate in these case, for it is possible to micromachine MgO [46, 47]. In some device concepts the pyroelectric thin film is first grown on a more ideal substrate than silicon, and later assembled on silicon [48, 49]. The initial substrate is dissolved or grinded down.

On silicon substrates, $PbTiO_3\{100\}$ films exhibit usually less than 50 % c-axis orientation. This phenomenon is accentuated if the deposition process yields a tensile stress, as can be caused by the crystallization shrinkage of the sol-gel preparation technique. Sputter processes allow incorporation of a compressive stress during in-situ deposition, and a hence stronger *c*-axis orientation [50]. The degree of orientation does not only influence the pyroelectric ceofficient, but also increases the dielectric constant, which renders the figures of merit even lower. The permittivity amounts to 80 to 120 in single-crystalline $PbTiO_3$ [51]. Thin films grown on silicon substrates, exhibit much larger values, typically 250, especially those processed by sol-gel techniques. In epitaxial films on MgO, this increase is well correlated with the degree of *c*-axis orientation (see Figure 11). According to these results, the dielectric constant of 250 corresponds to a degree of orientation of $^1/_3$, which is indeed observed in sol-gel films [52]. A possible origin of this behavior is the contribution of 90°-domain walls

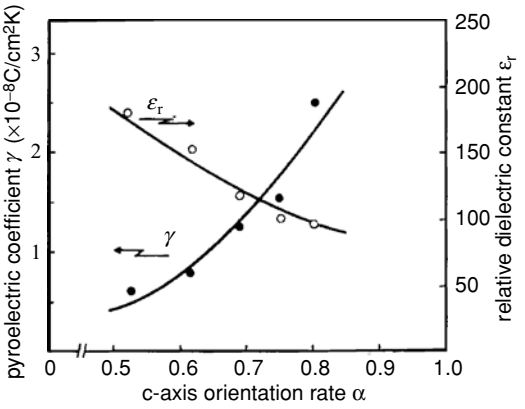

Fig. 11. Relation between pyroelectric coefficient γ, permittivity ε_r and the degree of a c-axis orientation of epitaxial $PbTiO_3$ thin films grown on Pt(100)/MgO(100), as obtained from θ-2θ x-ray diffraction experiments and defined as $\alpha = \frac{I(001)}{I(001)+I(100)}$([20]).

to the dielectric constant. Their density necessarily increases with lowering of the degree of *c*-axis orientation. The not so much convincing results with $\{100\}$-oriented films on silicon has motivated to chose the second best orientation, namely the (111)-orientation [53, 54]. However, it was found that optimized poling leads to about the same figures of merit for both orientations [55–57] since a portion of the a-domains can be flipped.

4.3. Piezoelectric contributions to pyroelectricity

In order to consider the third effect lest us briefly recall the definition of the pyroelectric coefficient. The "true" or primary pyroelectric effect is measured when volume and shape are kept constant (coefficient $p^{(strain)}$). This means that the thermal expansion is not included. The latter is causing the so-called secondary pyroelectric effect. When the pyroelectric effect is measured at constant stress ($p^{(stress)}$), what is usually done, it is composed of the primary and secondary effects:

$$p_3^{(stress)} = p_3^{(strain)} + e_{3i} \cdot \alpha_i \tag{4.1}$$

The thermal expansion coefficients α_i contribute to the measured charge through the piezoelectric effect, which in this case is described by the e_{ij}-coefficients. A thin film is free perpendicular to the plane (direction 3), but is forced to dilatate together with the substrate. With respect to free expansion, the film suffers a strain of $\alpha_s - \alpha_f$ (indexes s for substrate and f for film), given that film and substrate have a common temperature. This strain yields a stress which results in an additional secondary term that needs to be added to $p^{(stress)}$ [58]:

$$p_3^{(film)} = p_3^{(stress)} + \frac{2d_{31}}{s_{12}^E + s_{12}^E}(\alpha_s - \alpha_f). \tag{4.2}$$

$e_{31,f} = \frac{d_{31}}{s_{12}^E + s_{12}^E}$ is the effective piezoelectric coefficient of the thin film, which describes the charge density D_3 as a function of in plane strains [59]. Equation 3.9 can thus be derived from a thin film constituent equation that can be written as:

$$dD_3 = \varepsilon_{33}^{(x_1,x_2,\sigma_3,T)}\varepsilon_0 \cdot E_3 + p_3^{(stress)} \cdot dT + 2e_{31,f}^{(T)} \cdot (\alpha_s - \alpha_f) \cdot dT + e_{31,f}^{(T)} \cdot (x_1 + x_2) + d_{33,f}^{(T)} \cdot \sigma_3 \tag{4.3}$$

In perovskite based ferroelectric materials the contribution due to thermal mismatch is smaller than $p^{(stress)}$ [58]. Taking typical values for PZT films ($e_{31,f} = -2$ to -8 Cm^{-2}, $\alpha_s - \alpha_f = -4$ to 4 ppm/K) a piezoelectric contribution in the range of $+/-50$ $\mu Cm^{-2}K^{-1}$ is estimated. This value depends very much on the orientation of a tetragonal material. In some cases it might be negligible, in other cases it might be large.

4.4. Poling

There are two ways to deal with the poling issue: to apply a poling procedure on the finished device, or to grow self-poled films. The second possibility avoids a time consuming, and possibly also yield reducing production step. However, the growth of highly poled films works only with plasma or vacuum processes [61]. A charge gradient due to different diffusivities of electrons and oxygen vacancies after oxygen release in vacuum was given as possible origin [62]. The self-poling may also occur in sol-gel processed films, but is a too small effect. An optimal poling requires temperatures in the 100 to 200 °C range. The good pyroelectric materials often have too large coercive fields at room temperature for switching the polarization of the 180 ° domains. Large internal bias-fields indicate the existence of defect charges that pin domain walls and cause backswitching at zero field. At increased temperature, where the conductivity in the film is enhanced, these charges can be redistributed for pinning aligned domains. In the PZT 15/85 system the pyroelectric coefficient was observed to increase until 130 to 200 °C poling temperature (see Figure 12), above which some irreversible deterioration mechanisms take place. The dielectric constant decreases by about 30% during poling. In case of tetragonal PZT films it was observed that the c-axis domain volume fraction is enhanced at the cost of the a-axis domain part [56, 63].

4.5. Porosity and composites

Finally it has to be pointed out that not only perfect films in terms of microstructure, but also defective films may exhibit a good pyroelectric performance. The composite material of $BaTiO_3$ particles in a polymer matrix was an example encountered above. A further technique to dilute the ferroelectric material in order to decrease the dielectric constant was found in sol-gel processed PCT [64–66]. Porosity was installed due to a slow heating rate in the annealing step. In a randomly porous film one would also expect a decrease of the pyroelectric constant. This was, however, not necessarily observed. The dielectric constant decreases by almost a factor 3, whereas the pyroelectric coefficient stays about the same (see Figure 13), resulting in an increase of F_V"=p/ε to 3.4 μCm^2K^{-1} (using relative dielectric constant). A further improvement to 4.5 μCm^2K^{-1} was accomplished by introducing polymer particles into the solution [67]. These

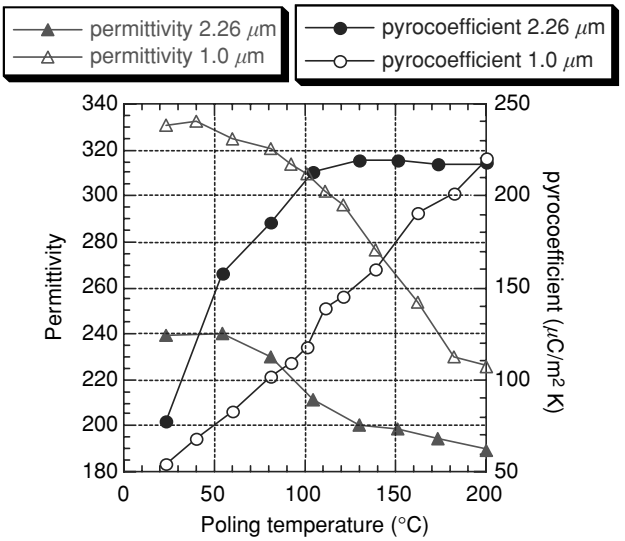

Fig. 12. Hot poling of sol-gel prepared PZT15/85 thin films with (111) orientation grown on $Pt(111)/Ta/Si_3N_4/SiO_2/Si$. Pyroelectric coefficient p and relative permittivity ε_r are shown as a function of poling temperature for two different films. A poling field of 2×10^7 V/m was applied. [55, 60]). The figure of merit F_V increases from 17 and 35 to 110 and 130 kV/m/K upon increasing the poling temperature from 25 to 200 °C.

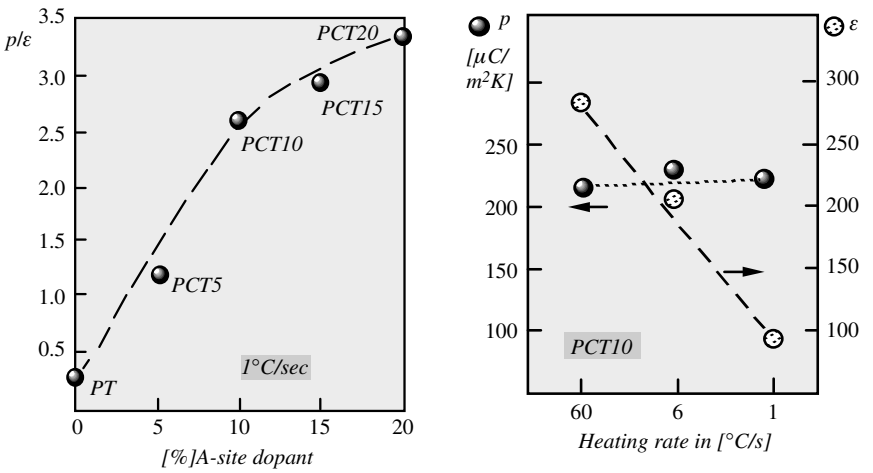

Fig. 13. Porous Ca modified $PbTiO_3$ obtained by sol-gel processing. The porosity °C is increased by slowing down the heating rate of the high-temperature anneal. Left: p/ε ration vs. Ca concentration. (The value 1 corresponds to a figure of merit F_V of 113 kV/m/K). Left: Pyroelectric coefficient p and permittivity ε as a function of heating rate (porosity). ([64, 66])

were burned away during annealing. An additional advantage of porosity is the lowering of thermal conductivity.

5. Micromachining

5.1. Fabrication technology

There are various fabrication concepts for pyroelectric devices. As discussed in the previous section, silicon is not the most suited substrate for pyroelectric thin film growth. On the other hand, silicon is the most suited (and cheapest) substrate for all other fabrication steps, such as semiconductor processing and micromachining. For this reason some concepts have been developed to grow the pyroelectric film on some other substrate and later glue it onto silicon structures, instead of directly depositing onto silicon wafers. Another variation is introduced by different methods of micromachining, which are needed for tailoring thermal properties. Small or linear arrays are rather fabricated by bulk micromachining, whereas large arrays have to be fabricated by surface micromachining techniques. An important question is finally whether the electronics should be integrated on the same chip, or whether a suitable packaging for hybrid assembly can be applied.

5.1.1. Silicon micromachining

The theory in section 4 showed the importance of the thermal insulation of the pyroelectric element. Silicon, which is best with respect to manufacturing and on-chip integration, is a very good thermal conductor. The pyroelectric element thus needs to be placed on some insulating supporting structure that is well isolated from the silicon, preferentially by a vacuum gap. There are various possibilities: membrane and bridge structures obtained by bulk micromachining, or bridge structures obtained by surface micromachining techniques. The schematic drawings of fig. 14 shows the three possibilities using wet etching. For all cases there are nowadays also dry etching (deep silicon dry etching) techniques allowing for fabrication of deep recessions with vertical walls and independently of the orientation of the feature with respect to the crystal planes. All of the possibilities have their convenient and their inconvenient aspects. Bulk micromachining works fine for small arrays and linear arrays, but the brittleness

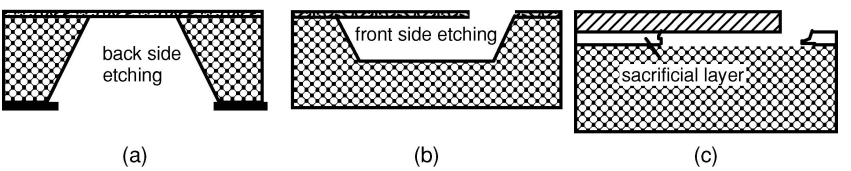

Fig. 14. Different micromachining techniques for thermal insulation of suspended structures: (a) bulk micromachining, (b) surface micromachining by front-side etching of the silicon substrate, (c) surface micromachining by sacrificial layers. The shown geometries in (a) and (b) correspond to anisotropic wet etching. (For a textbook, see e.g. [71].)

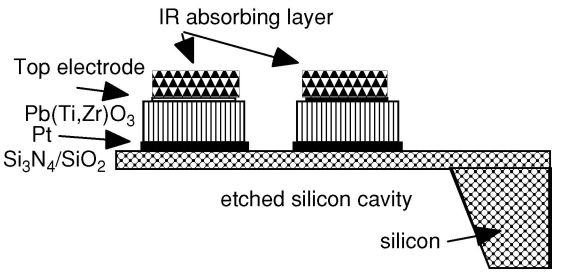

Fig. 15. Typical structure of pyroelectric elements of a linear array on a thin membrane fabricated by means of micromachining [75]. The elements are contacted to pads in the other direction than the one seen in this cut.

of the membrane poses problems for large two-dimensional arrays. Additionally, no transistors can be integrated in the pixel cell. Bridge structures exhibit a better thermal insulation than full membranes, but they need more advanced fabrication tools. Front side etching does not need double side aligning of masks, however, the masking of the devices during silicon etching can be a big obstacle when applying wet etching. This problem can be avoided by the use of an easily removable sacrificial layer. The latter is typically a layer of boron-phosphor-silicon glass (BPSG). Recently also porous silicon has been demonstrated for that purpose [68, 69]. A further possibility is the use of more or less isotropic dry etching of silicon in SF_6. With surface micromachining and sacrificial layer techniques, only small distances to the silicon substrate are achieved, making the use of vacuum imperative. Two-dimensional modelling of thermal properties of small gap structures is treated in [70]. It is not the goal of this section to go into details of silicon micromachining. The interested reader is referred the book of Madou [71] for an introduction into this topic.

Example 1: Membrane structure obtained by bulk micromachining for 1-d arrays

A stress compensated membrane layer of Si_3N_4/SiO_2 [72], or low stress nitride is coated on both sides of a double side polished wafer (see fig. 15). This coating fulfils the following functions: It serves as a mask for back-side etching in KOH or in an equivalent base (see, e.g. [73]). Second it serves as a support of the pyroelectric elements (membrane) exhibiting a low thermal conductivity. Bottom electrode and pyroelectric film (PZT15/85) are deposited by sputtering and sol-gel respectively. The top electrode is deposited and patterned by a lift-off technique before a quartz layer is sputter deposited for reduction of parasitic capacity below the contact pads [74]. Windows down to the top electrodes are opened by a CF_4 reactive ion etching. The PZT elements on the membrane part are etched free in a HCl:F solution, leaving only narrow bridges between the elements and the bulk silicon part, as needed for separation of bottom and top conductor. The platinum bottom electrode is removed between the elements by electrochemical etching. This etching technique does not attack the membrane material. After deposition and patterning of the conductor lines, pads (Au/Cr) and absorbing layer, the silicon is removed below the elements by back-side etching, as defined by a window in the back-side nitride layer, in order to obtain the result shown in Fig. 16. The 0.9 μm thick membrane with a specific conductivity of 2 W/m/K gives a fairly good thermal

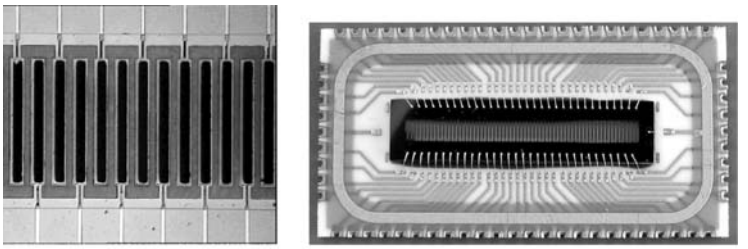

Fig. 16. (a) Top view on 50 element array with 200 μm period obtained with bulk micromachining showing the black platinum absorbers, the Cr-Au contact lines, the membrane layers between the elements, and the SiO_2 layer for reduction of parasitic capacitance (Membrane size: 2 × 11 mm) (from [76, 77]) (b) packaged 64 element array using same technology (Courtesy IR-Microsystems).

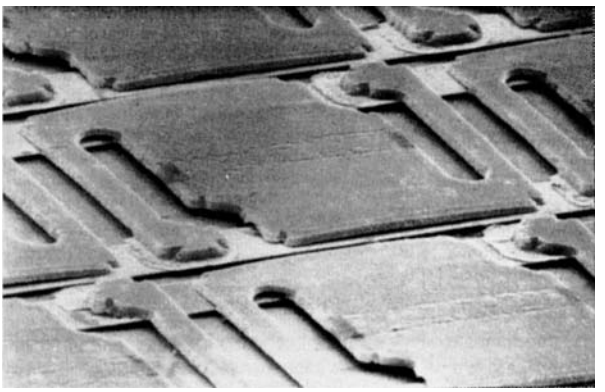

Fig. 17. Example of surface micromachining for focal plane arrays in monolithic technology, as designed for pyroelectric thin film focal plane array by GEC-Marconi. (from [53])

insulation, which allowed for rather high voltage responses at 1 Hz of 800V/W in air [75]. The membrane roughly doubles the heat capacity of the pyroelectric element. Rather long thermal time constants of 28 ms in air, and 104 ms in vacuum have been obtained with such devices [16].

Example 2: Surface micromachining for 2-d arrays

For 2 dimensional arrays bulk micromachining is not practicable. Suitable surface micromachining processes are thus required. The example presented here [53] is based on 0.5 μm silicon nitride layer on a 1 to 2 μm thick sacrificial layer. The silicon nitride is the mechanical supporting layer for the pyroelectric capacitor stack. After removal of the sacrificial layer, the suspended structure is hold by two bridges (see Figure 17). The geometrical arrangement combines in an optimal way the need for long bridges on one hand and the need for an as large as possible detector density (filling factor). The extremities of the bridges rest on previously prepared via hole studs, which also serve

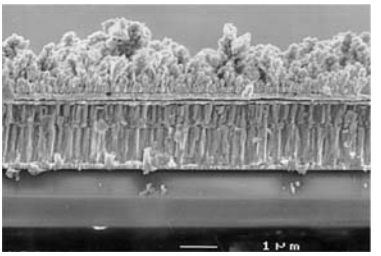

Fig. 18. Electro-chemically deposited black platinum grown on a Cr-Au top electrode on a PZT/Pt/Ta/Si_3N_4/SiO_2 layer stack [16].

to contact bottom and top electrode. The CMOS processing for the readout electronics, including the conductor lines to the transistors, must be performed before ferroelectric film processing and micromachining is carried out. This poses one of the major problems since the high processing temperatures for pyroelectric films usually exceed the stability limit of the standard aluminum conductor lines used in CMOS technology.

5.2. IR absorption techniques

There are several possibilities for increasing the absorption of the IR light. One is the addition of a black absorbing layer. Very high absorption coefficients are obtained by this method. Electrochemically deposited black platinum [78] yields 90 % absorption up to 10 μm wavelength. The blackness results from the dendritic and porous microstructure (see Figure 18). There is also the possibility to produce black gold by evaporation in a nitrogen atmosphere. For good absorption, a thickness of about 1 to 2 μm is needed. This is quite a lot compared to the pyroelectric film thickness and leads to an enhancement of the heat capacity, and consequently to a reduction of the current response. The black absorbing layer is thus ideal for low frequency, voltage detection applications.

A second method applies very thin, semi-transparent Nickel or Cr-Ni films as absorbing top electrodes. The absorption depends on the refractive indices on the two sides of the metal film, and of the absorption coefficient of the latter [79, 80]. On PVDF absorptivities of 0.6 (@ 8–14 μm) have been achieved. The formulas given by Bauer and coworkers indicate that the high refractive index of ferroelectric materials might reduce this value to 0.4 to 0.5.

The third method profits from the fact that a transparent layer of λ/4 thickness on a totally reflecting substrate (e.g. a metal) exhibits a low reflection coefficient for the wavelength 1. The wave is entrapped in the λ/4 cavity and absorbed during multiple reflections. Taking the pyroelectric film as this transparent material, about 1.0 μm ($n = 2.6$) thickness would be needed for 10 μm wavelength. This thickness is ideal for growing high quality thin films at reasonable costs by various deposition techniques. This method requires a transparent top electrode, for which usually a very thin, semitransparent metal film is applied. It is clear that this method can be combined with the previous one [81]. A further modification of this method is the combination with the micromachined surface gap [82]. The bottom of the gap is formed by a mirror (e.g. a metal film) and the cavity consists of the vacuum gap and the pyroelectric thin film, which now

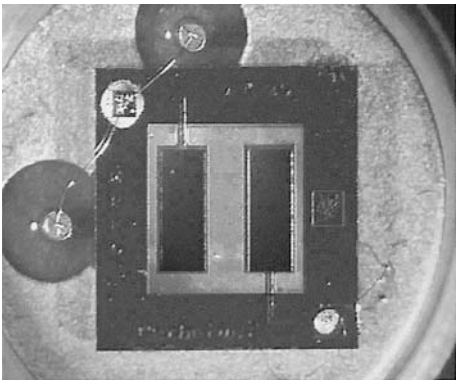

Fig. 19. Top view on point detector, mounted on TO-39 header. The dice is 4.5 × 4.5 mm large. Two rectangular pyroelectric elements are sitting on a transparent membrane. A JFET is glued onto the dice at the upper left corner. (from [16]).

must be thinner than a micrometer. In addition, a transparent bottom electrode must be provided.

5.3. Connection to read-out chip

In order to exploit the noise limit of the sensor element, the electrical connections to the first amplification stage of the electronics have to be as short as possible. The ideal solution is certainly the monolithic integration, i.e., a direct integration of sensors and read-out electronics. However, this increases very much the complexity of fabrication. As a consequence, the yield goes down, and the costs go up. For point detectors and linear arrays, the hybrid approach is certainly the more efficient and cheaper method. In the case of point detectors, the necessary preamplifier, a simple JFET, finds place in one corner of the sensor dice (see Figure 19).

In case of (large) two-dimensional arrays the vertical stacking of detector elements and read-out circuit is inevitable. In order to achieve a good filling factor, the detector elements have to cover most of the surface. There is hardly any place for horizontal electrical interconnects on the same level. Two concepts are conceivable: Either the detector structure is obtained by surface micromachining on top of the read-out wafer, or the detector array is fabricated on a different wafer and joined later to the read-out wafer by a suitable bonding technique assuring vertical electrical contacts. The second possibility is a stacked wafer configuration. Deep silicon etching techniques also contributed to this field. It is possible to etch vertical holes through a complete waver (300 to 400 μm) that exhibit smaller diameters than the pitch of the array (40 to 50 μm). The holes can be filled with a conductor (doped poly-Si deposited by CVD, electrochemically deposited Ni or Cu) providing for a contact between surface micromachined thermal structures on one side, and a ROIC wafer joined on the other side by flip chip techniques. No such 2-d stacked thin film detector exists yet, but some inspiration can be gained from reticulated ceramic detectors. Quite complex hybrid focal plane arrays with

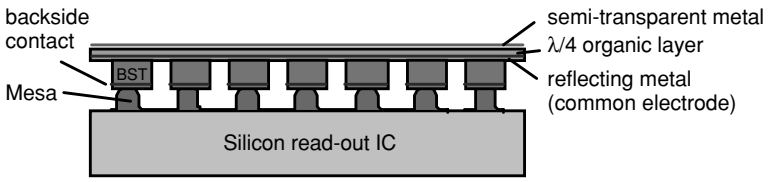

Fig. 20. Schematic cross section through focal plane array obtained by reticulation of ceramic BST wafer that is grinded down and bonded to the read-out chip by a mesa structure (TI uncooled FR hybrid technology [84].) The pixel thickness (BST) amounts to 10 to 18 μm, the pitch is 48.5 μm.

384 × 288 and 328 × 245 pixels were recently presented by GEC-Marconi and Texas Instruments [83, 84]. They work either with pyroelectric PZT ceramic or with field-induced pyroelectricity (dielectric bolometer) of $BaSrTiO_3$ (BST) or $PbSc_{1/2}Ta_{1/2}O_3$. The version of Texas Instruments operates with BST at a stabilized temperature near the ferroelectric critical temperature around 20 °C. It is still called an uncooled imaging device, because the necessary heater/Peltier element combination consumes much less power than is required for the standard cooled devices. The starting point of fabrication is a ceramic BST wafer. After reticulation by laser or ion milling processes, polishing down, electrode and absorber layer deposition, the so obtained BST array is bonded to a read-out IC via a mesa structure (see Figure 20) (GEC-Marconi utilizes solder bumps). The absorber layer is a transparent organic λ/4 layer, sandwiched between a semitransparent metal layer and the common electrode. The mesa structure is grown on the read-out IC. The latter is either a charge-coupled device (CCD) or exhibits amplifiers and sample-and-holds for each pixel, combined with a multiplexed reading for the output. Such devices achieve a NETD of 0.1 K or less.

The performance of the above hybrid FPA's is very sufficient at present. Today they are inside many commercial products. However, thermal properties are not optimal yet: the heat capacity of the ceramic pixel is about ten times larger than with a thin film pixel. Also the heat conduction through the mesa studs is certainly larger than what could be achieved with silicon micromachining. So it is expected that thin film versions still could improve the performance and reduce costs.

6. Applications

There are, in fact, only few reported works, where a complete device has been manufactured and characterized. Most of the industrial thin film array projects are currently in an intermediate stage of development or in the stage to be introduced into the market. So quite some time elapsed after the first work of Schopf, Ruppel and Würfel with $NaNO_2$ thin films in 1989 [85].

Point detectors

The point detector shown in Figure 19 is the simplest of all devices. No special electronics was needed. The sensor dice simply replaced the $LiTaO_3$ single crystal

detector. The thin film version was able to detect a moving person on a distance of maximal 30 m [16, 86]. The relatively large flakes resulted in a large thermal coupling by convection, reducing the D^* to 1.0×10^8 cmHz$^{1/2}$/W. Point detectors are in general too simple devices to justify micromachined thin film versions.

A linear array working with MgO substrates has been developed by Matsushita [87]. PLT thin films were deposited onto MgO(100) substrates. These were later etched from the backside to obtain the desired thermal properties, similar to silicon bulk micromachining. A detectivity of 3.5×10^8 cmHz$^{1/2}$/W was measured.

Linear arrays

The linear array shown in Figure 16 has been developed for an infrared spectroscopy gas sensor. IR-light source, optics, focal plane array and read-out electronics are integrated in one housing. The light source is a filament or a micromachined thermal infrared source. The heater current is modulated to obtain a modulation of the signal. Each element of the array receives a certain wavelength section, as defined by a grating. In this way a complete absorption spectrum can be sampled in parallel operation [89]. Interesting wavelength intervals are the range between 8 and 12 μm for hydrocarbons and between 4 to 5 μm for carbon oxides (see Figure 21). The pyroelectric material was a sol-gel deposited, (111)-oriented PZT15/85 thin film. With a chopping frequency of 10 Hz (measurement bandwidth of 1.25 Hz) a NEP of 0.2 nW and a detectivity of 2×10^8 cmHz$^{1/2}$/W was measured after the CMOS readout chip [88]. The read-out chip increased the noise by about 30 %.

Pyroelectric 2-d focal plane arrays

Development of pyroelectric focal plane arrays started in the 1980's. A device consisting of a reticulated, 60 μm thick pyroelectric ceramic wafer that was bonded to a CCD readout wafer by means of contact solder bumps, exhibiting a pixel diameter of 70 μm showed a NETD of 400 mK at 25 Hz [2, 90]. A presently sold commercial product consists of a 14 μm thick reticulated ceramic wafer with a 50 μm pitch [91], as shown in Figure 20. The NETD could be reduced to 75 mK, and the spatial resolution could be

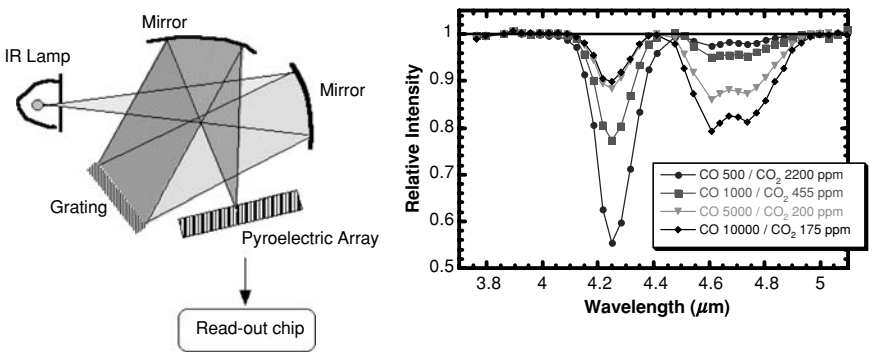

Fig. 21. Absorption spectra of CO_2 and CO mixtures measured by means of a thin film pyroelectric array (from [89]).

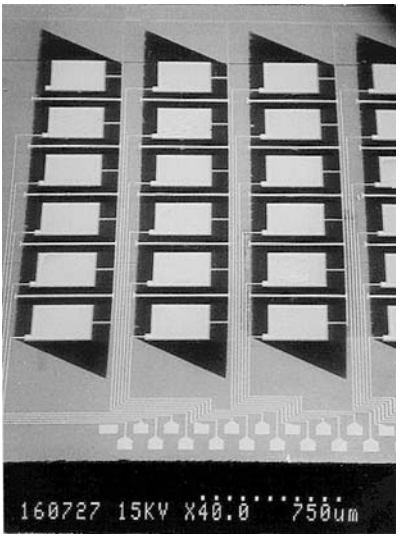

Fig. 22. View on 11 × 6 array of Siemens [92].

increased. The fundamental limits are not yet reached with this camera. However, in the frame of this ceramic wafer technology, a further shrinkage of wafer thickness and pitch will become increasingly difficult. Much more promising are silicon micromachining techniques enabling still smaller and thinner pixels. Thermal cross talk between pixels is reduced very much as well.

Siemens has developed an 11 × 6 array for thermal imaging (see Figure 22) potentially useful for small security cameras. Sputter deposited PZT 20/80 films were applied and D* of 3×10^8 cmHz$^{1/2}$/W is reported for 10 Hz. The suspended structures have been obtained by bulk micromachining of (110) silicon wafers. This silicon cut allows fabrication of narrower silicon bridges, which are needed in this design for carrying the electrical connection lines to the pads to which the read-out electronics is connected [92].

Raytheon-TI Systems reported the successful development of a monolithically integrated focal plane array based on a pyroelectric PLZT thin film, and containing 320 × 240 pixels of 50 × 50 μm size [82, 91, 93]. Crucial to this achievement was the balancing of the thermal budget of the sol-gel deposition process to allow perovskite PLZT crystallization on the one hand, and to avoid degradation of the aluminum metallization on the other hand. This allowed the fabrication of the sensor structure directly on top of the interconnecting metal level of the CMOS read-out circuit. The critical temperature for the CMOS metallization was evaluated to be 550 °C during short anneals. The sensor structure consisted of suspended pyroelectric thin film plates obtained by a sacrificial layer technique (see Figs. 23 and 24) similar to the structure shown in fig. 18), with the difference that the gap is used to trap the IR light as discussed above. Thermal imaging with a NETD of around 200 mK has been demonstrated. This value is higher than expected from basic pyroelectric and thermal properties. Major problems in transferring processes from the laboratory stage to a complex device fabrication have

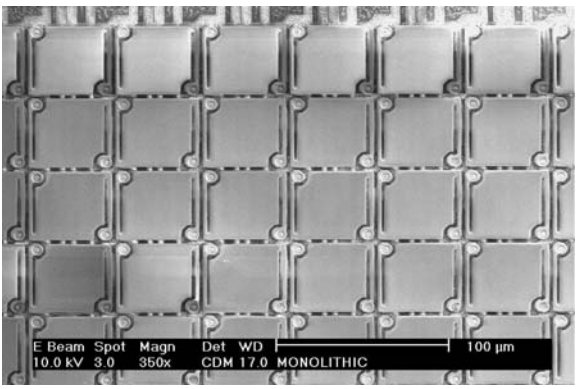

Fig. 23. Partial view on 320 × 240 pixel array of Raytheon Systems (from [94]) (Courtesy Raytheon Systems).

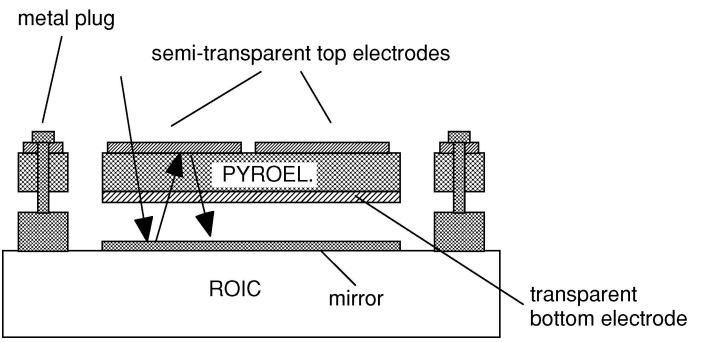

Fig. 24. Schematic cross section through pyroelectric IR detector pixel of Raytheon systems (after [82]). One pixel consists of two serial capacitors facilitating the fabrication.

been encountered. Film stresses, cracking, warping, metal oxidation and interdiffusion reactions resulted in a lowering of pyroelectric properties and absorption coefficient.

It has also been tried to avoid micromachining completely by applying silica aerogels as thermal insulation layer [95]. A NETD of 700 mK was reported. The problem is essentially that at 30 Hz the thermal wavelength in such an aerogel amounts still to about 20 µm (see section 3). With a thickness of 1 µm, the heat conductivity is about a factor of 10 higher than with bulk micromachined membrane structures in air (as estimated from aerogel data given in [96]). The increase of the aerogel layer thickness is problematic since the surface becomes more and more rough. A further problem is the limitation of the processing temperature to less than 600 °C at which the aerogel starts to collapse.

In the previous discussion, the NETD was taken as measure of performance. However, this is not the only one. Crosstalk, dynamic range, fix pattern noise, minimum resolvable temperature, and smallest resolvable feature are other important parameters. The human eye reacts also differently on dc-coupled (as e.g. thermoresistive bolometers)

devices and ac-coupled devices (as e.g. pyroelectrics). The picture quality in the latter case appears to be better than in the first case, even though the NETD is equal [82].

7. Conclusions

This article reviewed the status of research in pyroelectric thin films, of pyroelectric thin film devices and applications. The sensitivity limit of pyroelectric IR detectors was derived and several ways of improving the present performance for approaching the theoretical limits were pointed out. It must be pointed out that fundamental limits of thermal detectors, as achievable by micromachining techniques in general, could also be reached by pyroelectric micromachined versions. In principle, micromachined thin film versions could decrease the NETD down to 10–20 mK^5. Unfortunately there are still too many processing difficulties to surmount. Quite some materials engineering combined with thin film processing skills are still required to improve the relevant figures of merits. This includes not only an increase of the pyroelectric coefficient, but also a decrease of dielectric constant and dielectric loss. The material to be used, or whether the true or the induced pyroelectric effect should be applied are still open questions. On the device side, integration technology is of paramount importance for achieving the optimal combination with the required thermal properties and the needs for electrical read-out. Many things will depend on the practicability of fabrication. Pyroelectricity has good prerequisites for use in high-end thermal detectors. However, the mastery of fabrication is the key for obtaining competitive pyroelectric devices.

References

[1] S.G. Porter, A brief guide to pyroelectric detectors, *Ferroelectrics* 33, 193–206 (1981)
[2] R.W. Whatmore, Pyroelectric devices and materials, *Reports on progress in physics* 49, 1335–1386 (1986)
[3] S. Bauer and S.B. Lang, Pyroelectric polymer electrets, *IEEE Trans. Dielectrics Electr. Insulation* 3, 647–676 (1996)
[4] R.G. Buser and M.F. Tompsett, *Historical overview*, in *Uncooled infrared imaging arrays and systems*, P.W. Kruse and D.D. Skatrud, Editors. 1997, Academic Press. p. 1–16.
[5] P. Muralt, Micromachined infrared detectors based on pyroelectric thin films, *Rep. Progr. Phys.* 64, 1339–1388 (2001)
[6] S.B. Lang, *Sourcebook of pyroelectricity*. 1974, Lonon: Gordon and Breach Science Publishers.
[7] S. Tinte, J. Iniguez, K.M. Rabe, and D. Vanderbilt, Quantitative analysis of the first principles effective Hamiltonian approach to ferroelectric perovskites, *Phys. Rev. B* 67, 064106 (2003)
[8] Y.F. Nye, *Physical properties of crystals*. 1985: Oxford University Press.
[9] R. Watton and M.A. Todd, Induced pyroelectricity in sputtered lead scandium tantalate films and their merit for IR detector arrays, *Ferroelectrics* 118, 279–295 (1991)
[10] M.E. Lines and A.M. Glass, *Principles and applications of ferroelectrics and related materials*. 1977, Oxford: Oxford University Press.
[11] F. Chu, N. Setter, and A.K. Tagantsev, The spontaneous relaxor-ferroelectric transition of PST, *J. Appl. Phys.* 74, 5129–5134 (1993)

[12] M. Daglish, A dynamic method for determining the pyroelectric response of thin films, *Integrated Ferroelectrics* 22, 473–488 (1998)
[13] A.K. Tagantsev, Mechanisms of dielectric loss in microwave materials, *MRS Symp. Proc.* 603, 221–232 (2000)
[14] V.L. Gurevich and A.K. Tagantsev, Intrinsic dielectric loss in crystals, *Adv. Physics* 40, 719–767 (1991)
[15] E.H. Putley, The pyroelectric detector, *Semiconductors and Semimetals* 5, 259–285 (1970)
[16] M. Kohli, C. Wüthrich, K.G. Brooks, B. Willing, M. Forster, P. Muralt, et al., Pyroelectric thin film sensor array, *Sensors and Actuators A* 60, 147–153 (1997)
[17] J.M. Lloyd, *Thermal imaging systems*. Optical physics and Engineering, ed. W.L. Wolfe. 1975: Plenum Press.
[18] P.W. Kruse, Uncooled IR focal plane arrays, *SPIE* 2552, 556–563 (1995)
[19] P.W. Kruse, A comparison of the limits to the performance of thermal and photon detector imaging arrays, *Infrared Physics & Technology* 36, 869–882 (1995)
[20] K. Iijima, Y. Tomita, R. Takayama, and I. Ueda, Preparation of c-axis oriented PbTiO3 thin films and their crystallographic, dielectric, and pyroelectric porperties, *J. Appl. Phys.* 60, 361–367 (1986)
[21] A.J. Moulson and J.M. Herbert, *Electroceramics*. 1990, London: Chapman & Hall.
[22] V. Fuflyigin, E. Salley, P. Vakhutinsky, A. Osinsky, and J. Zhao, Free-standing films of PST for uncooled infrared detectors, *Appl. Phys. Lett.* 78, 365–367 (2001)
[23] A.P.D. Kroon, S.C. Dunn, and R.W. Whatmore, Piezo and pyroelectric properties of lead scandium tantalate thin films, *Integrated Ferroelectrics* 35, 209–218 (2001)
[24] Z. Kighelman, D. Damjanovic, A. Seifert, L. Sagalowicz, and N. Setter, Relaxor behavior and electromechanical properties of Pb(Mg,Nb)O3 thin films, *Appl. Phys. Lett.* 73, 2281–83 (1998)
[25] D. Liu and D. Payne, Lower temperature crystallization and ordering in sol-gel derived PST powerders and thin layers, *J. Appl. Phys.* 77, 3361–64 (1995)
[26] D. Liu and H. Chen, Low-temperature preparation of perovskite PST thin films using MOCVD, *Materials Letters* 28, 17–20 (1996)
[27] C.E. Murphy and P.J. Dobson, Pyroelectric properties of fine BaTiO3 PVDFT thin film composites, *Ferroelectrics* 152, 127–132 (1994)
[28] H. Vogt, P. Würfel, U. Hetzler, and W. Ruppel, NaNO2 layers as pyroelectric radiation detectors, *Ferroelectrics* 33, 243–248 (1981)
[29] C.-H. Kohli, P.E. Schmid, and F. Lévy. *Ferro- and pyroelectric properties of LiTaO3 thin films*. in *IMF-9*. 1997. Séoul.
[30] C.K. Kwok and S.B. Desu, Formation kinetics of PZT thin films, *J. Mater. Res.* 9, 1728–1733 (1994)
[31] K. Aoki, Y. Fukuda, K. Numata, and A. Nishimura, Effects of titanmium buffer layer on PZT crystallization porecess in sol-gel deposition technique, *Jpn. J. Appl. Phys.* 34, 192–195 (1995)
[32] P. Muralt, T. Maeder, L. Sagalowicz, S. Hiboux, S. Scalese, D. Naumovic, et al., Texture control of PbTiO3 and PZT thin films with TiO2 seeding, *J. Appl. Phys.* 83, 3835–3841 (1998)
[33] T. Maeder, P. Muralt, M. Kohli, A. Kholkin, and N. Setter, Pb(Zr,Ti)O_3Thin Films by In-situ Reactive Sputtering on Micromachined Membranes for Micromechanical Applications, *British Ceram. Proc.* 54, 206–218 (1995)
[34] A. Seifert, N. Ledermann, S. Hiboux, and P. Muralt, Study of the transverse piezoelectric coefficient of PZT thin films as a function of texture and composition, *Mat. Res. Soc. Symp. Proc.* 596, 535–540 (2000)

[35] A.L. Roitburd, Equilibrium structure of epitaxial layers, *phys. stat. sol.(a)* 37, 329–339 (1976)

[36] C.M. Foster, Z. Li, M. Buckett, D. Miller, P.M. Baldo, L.E. Rehn, et al., Substrate effects on the structure of epitaxial PbTiO3 thin films prepared on MgO, LaAlO3, and SrTiO3 by metallorganic chemical vapor deposition, *J. Appl. Phys.* 78, 2607–2622 (1995)

[37] C.M. Foster, W. Pompe, A.C. Daykin, and J.S. Speck, Relative coherency strain and phase transformation history in epitaxial ferroelectric thin films, *J. Appl. Phys.* 79, 1405–1415 (1996)

[38] W. Pompe, X. Gong, Z. Suo, and J.S. Speck, Elastic energy release due to domain formation in the strained epitaxy of ferroelectric and ferroelastic thin films, *J. Appl. Phys.* 74, 6012–6019 (1993)

[39] A. Seifert, A. Vojta, J.S. Speck, and F.F. Lange, Microstructural instability of single crystal thin films, *J. Mater. Res.* 11, 1470–1582 (1996)

[40] J.S. Speck and W. Pompe, Domain configurations due to multiple misfit relaxation mechanisms in epitaxial ferroelectric films I. Theory, *J. Appl. Phys.* 76, 466–476 (1994)

[41] J.S. Speck, A. Seifert, W. Pompe, and R. Ramesh, Domain configurations due to multiple misfit relaxation mechanisms in epitaxial ferroelectric films II: Experimental verification and implications, *J. Appl. Phys.* 76, 477–483 (1994)

[42] J.S. Speck, A.C. Daykin, A. Seifert, E.A. Romanov, and W. Pompe, Domain configurations due to multiple misfit relaxation mechanisms in epitaxial ferroelectric films III: Intefacial defects and domain misorientations, *J. Appl .Phys.* 78, 1696–1706 (1994)

[43] N.A. Pertsev and A.G. Zembilgotov, Domain population in epitaxial ferroelectric thin films: Theoretical calculations and comparison with experiment, *J. Appl. Phys.* 80, 6401–6406 (1996)

[44] E. Sviridov, V. Alyoshin, Y. Golovko, I. Zakharchenko, V. Mukhortov, and V. Dudkevich, Phase transition and domain structure of heteroepitaxial PbTiO3/(001) MgO films, *Ferroelectrics* 128, 1–6 (1992)

[45] A. Seifert, F.F. Lange, and J.S. Speck, Epitaxial growth of PbTiO3 thin films on (001) SrTiO3 from solution precursors, *J. Mater. Res.* 10, 680–691 (1995)

[46] K. Iijima, N. Nagao, T. Takeuchi, I. Ueda, Y. Tomita, and R. Takayama, Sputtering of lead-based ferroelectrics, *MRS Symp. Proc* 310, 455–465 (1993)

[47] T. Kotani, T. Nakanishi, and K. Nomura, Fabrication of a new pyroelectric infrared sensor using MgO surface micromachining, *Jpn. J. Appl. Phys.* 32, 6297–6300 (1993)

[48] Z. Sitar, R. Gutmann, H. Pierhöfer, and P. Günter. *Liquid phase epitaxy of Na-K-Ta-Nb-O for pyroelectric applications*. in *MRS Symposium*. 1995. Boston: MRS.

[49] R. Takayama and etal. in *ISIF*. 1995.

[50] P. Muralt. *Piezoelectric and pyroelectric microsystems based on ferroelectric thin films*. in *10th IEEE Symp.Appl.Ferroelectrics*. 1996. East Brunswick (USA): IEEE.

[51] Z. Li, M. Grimsditch, X. Xu, and S.K. Chan, The elastic, piezoelectric and dielectric constants of tetragonal PbTiO3 single crystals, *Ferroelectrics* 141, 313–325 (1993)

[52] Y.H. Huang, *Sol-gel PbTiO3 thin films for pyroelectric applications*. 1995, Swiss Fed.Inst.Technology: Lausanne.

[53] N.M. Shorrocks, A. Patel, M.J. Walker, and A.D. Parsons, Integrated thin film PZT pyroelectric detector arrays, *Microelectronic Eng.* 29, 59–66 (1995)

[54] M. Kohli, C. Wüthrich, K. Brooks, M. Forster, P. Muralt, N. Setter, et al. *Pyroelectric thin film sensor array*. in *Eurosensors*. 1996. Leuven (Belgium).

[55] M. Kohli, A. Seifert, and P. Muralt, Poling of pyroelectric thin films, *J. Integrated Ferroelectrics* 22, 453–463 (1998)

[56] M. Kohli, P. Muralt, and N. Setter, Removal of 90°-domain pinning in (100) PZT 15/85 thin films by pulsed operation, *Appl. Phys. Lett.* 72, 3217–19 (1998)

[57] M. Kohli and P. Muralt, Poling of ferroelectric films, *Ferroelectrics* 225, 155–162 (1998)
[58] J.D. Zook and S.T. Liu, Pyroelectric effects in thin film, *J. Appl. Phys.* 49, 4604–4606 (1978)
[59] P. Muralt, Piezoelectric thin films for MEMS, *Integrated Ferroelectrics* 17, 297–307 (1997)
[60] M. Kohli, A. Seifert, B. Willing, K. Brooks, and P. Muralt, Thin film pyroelectric arrays as infra-red detectors, *J. Int. Ferroelectrics* 17, 359–367 (1997)
[61] R. Bruchhaus, D. Pitzer, R. Primig, W. Wersing, and Y. Xu, Deposition of self-polarized PZT films by planar multi-target sputtering, *Integrated Ferroelectrics* 14, 141–149 (1997)
[62] G.E. Pike, W.L. Warren, D. Dimos, B.A. Tuttle, R. Ramesh, J. Lee, et al., Voltage offsets in (Pb,La)(Zr,Ti)O3 thin films, *Appl. Phys. Lett* 66, 484–486 (1995)
[63] H. Hector, N. Floquet, J.C. Niepce, P. Gaucher, and J.P. Ganne, Texture, structure and domain microstructure of ferroelectric PZT thin films, *Microelectronic Eng.* 29, 285–288 (1995)
[64] A. Seifert, P. Muralt, and N. Setter. *Ca-modified PbTiO3 thin films for pyroelectric devices*. in *Electroceramics V*. 1996. Aveiro (Portugal): University of Aveiro.
[65] A. Seifert, L. Sagalowicz, P. Muralt, and N. Setter, Microstructural evolution of dense and porous (PbCa)TiO3 thin films for pyroelectric applications, *J. Mater. Res.* 14, 2012–2022 (1999)
[66] A. Seifert, P. Muralt, and N. Setter, High figure of merit porous (Pb,Ca)TiO3 thin films for pyroelectric applications, *Appl. Phys. Lett.* 72, 2409–11 (1998)
[67] G. Suyal, A. Seifert, and N. Setter, Pyroelectric nanoporous films: Synthesis and properties, *Appl. Phys. Lett.* 81, 1059–1061 (2002)
[68] T. Bischoff, G. Müller, W. Welser, and F. Koch, Frontside micromachining using porous silicon sacrificial layer technologies, *Sensors and Actuators A* 60, 228–234 (1997)
[69] C. Dücsö, E. Vazsonyi, M. Adam, I. Szabo, I. Barsony, J.G.E. Gardeniers, et al., Porous silicon bulk micromachining for thermally isolated membrane formation, *Sensors and Actuators A* 60, 235–239 (1997)
[70] B. Ploss, D. Lienhard, and F. Sieber, Thermal simulation of micromachined bridges for integrated pyroelectric sensor arrays, *Microelectronic engineering* 29, 75–78 (1995)
[71] M. Madou, *Fundamentals of microfabrication*. 1997, Boca Raton: CRC Press.
[72] A. Bell, Y. Huang, O. Paul, Y. Nemirovsky, and N. Setter, A thin film pyroelectric detector, *Int. Ferroelectrics* 6, 231–240 (1995)
[73] H. Seidel, A. Heuberer, and H. Baumgärtel, *J. Electrochem. Soc.* 137, 3612 (1990)
[74] M.-A. Dubois and P. Muralt, PZT thin film actuated elastic fin micromotor, *IEEE Trans. Ultrasonics, Ferroelectrics, and Frequency Control* 45, 1169–1177 (1998)
[75] P. Muralt, K. Brooks, M. Kohli, T. Maeder, and C. Wüthrich. *Ferroelectric thin films for microsystems*. in *ECASIA*. 1995. Montreux (Switzerland): John Wiley & Sons.
[76] B. Willing, M. Kohli, P. Muralt, N. Setter, and O. Oehler. *Gas spectrometry based on pyroelectric thin film arrays integrated on silicon*. in *Transducers—International Conf. on Solid- State Sensors and Actuators*. 1997. Chicago.
[77] B. Willing, M. Kohli, P. Muralt, N. Setter, and O. Oehler, Gas spectrometry based on pyroelectric thin film arrays integrated on silicon, *Sensors and Actuators A* 66, (1998)
[78] W. Lang, K. Kühl, and H. Sandmeier, Absorbing layers for thermal infrared detectors, *Sensors and Actuators A* 34, 243–248 (1992)
[79] D. Lienhard, F. Heepmann, and B. Ploss, Thin Nickel films as absorbers in pyroelectric sensorarrays, *Microelectronic Eng.* 29, 101–104 (1995)
[80] S. Bauer, S. Bauer-Gogenea, and B. Ploss, *Appl. Phys. B* 54, 544 (1992)
[81] K.C. Liddiard, Application of interferometric enhancement to self-absorbing thin film thermal IR detectors, *Infrared Phys.* 34, 379–387 (1993)
[82] C.M. Hanson, H.R. Beratan, and J.F. Belcher. *Uncooled infrared imaging using thin film ferroelectrics*. in *Infrared detectors and focal plane arrays VI*. 2000. San Jose: SPIE.

[83] R. Watton, P.A. Manning, M.J. Perkins, and J.P. Gillham. *Uncooled IR imaging: hybrid and integrated bolometer arrays*. in *Infrared technology and applications XXII*. 1996. Orlando: SPIE.

[84] R. Owen, J. Belcher, H. Beratan, and S. Frank. *Reproducibility advances in hybrid uncooled infrared devices II*. in *Infrared detectors and focal plane arrays IV*. 1996. Orlando, Florida: SPIE.

[85] H. Schopf, W. Ruppel, and P. Wuerfel, 16-element linear pyroelectric array with NaNO2 thin films, *Infrared Physics* 29, 101–106 (1989)

[86] M. Kohli, Y. Huang, T. Maeder, C. Wüthrich, A. Bell, P. Muralt, et al., Processing and properties of thin film pyroelectric devices, *Microelectronic Engineering* 29, 93–96 (1995)

[87] S. Fujii, T. Kamata, S. Hayashi, Y. Tomita, R. Takayama, T. Hirao, et al. *Pyroelectric linear infrared sensors made of La-modified PbTiO3 thin films and their applications*. in *SPIE*. 1995: SPIE.

[88] B. Willing, P. Muralt, T. Reimann, and O. Oehler. *High end pyroelectric thin film array detector system*. in *Transducers'99*. 1999. Sendai (Japan).

[89] B. Willing, M. Kohli, P. Muralt, and O. Oehler, Thin film pyroelectric array as a detector for and infrarted gas spectrometer, *Infrared Physics and Technology* 39, 443–449 (1998)

[90] R. Watton, F.W. Ainger, S. Porter, D. Pedder, and J. Gooding. in *Infrared technology X*. 1984: SPIE.

[91] C.M. Hanson, H.R. Beratan, J.F. Belcher, K.R. Udayakumar, and K.L. Soch. *Advances in monolithic ferroelectric uncooled IRFPA technology*. in *SPIE: Infrared detectors and focal plane arrays V*. 1998. Orlando, Florida: SPIE.

[92] R. Bruchhaus, D. Pitzer, R. Primig, M. Schreiter, W. Wersing, G. Hofmann, et al. *11 × 16 elementiges Pyrodetektorarray auf der Basis gesputterter selbstpolarisierter PZT-Dünnschichten*. in *5th Infrared Sensors and Systems*. 1997. Dresden: Dresden University Press.

[93] H.R. Beratan, C.M. Hanson, J.F. Belcher, and K.R. Udayakumar. *Thin film pyroelectric imaging array*. in *International Symposium on Integrated Ferroelectrics (ISIF)*. 1998. Monterey (CA).

[94] C.M. Hanson, H.R. Beratan, J.F. Belcher, K.R. Udayakumar, and K. Soch, *Next-generation ferroelectric uncooled IR detectors*. 1998, Rytheon Systems Company.

[95] J.A. Ruffner, P.G. Clem, B.A. Tuttle, C.J. Brinker, C.S. Sriram, and J.A. Bullington, Uncooled thin film infrared imaging device with aerogel thermal insulation: deposition and planarization techniques, *Thin Solid Films* 332, 356–361 (1998)

[96] P. Scheuerpflug, M. Hauck, and J. Fricke, Thermal properties of silica aerogels between 1.4 and 300 K, *J. Non-Cryst. Solids* 145, 196–201 (1992)